Effects of Manufacturing Imperfections in Concentrated Coil Axial Flux PM Machines: Evaluation and Tests

I. INTRODUCTION

A XIAL FLUX (AF) Permanent Magnet Synchronous Machines (PMSM) exhibit a high torque capability [1]-[2]; however they are rather sensitive to geometrical imperfections. In fact, the "pancake" structure implies that even a small unforeseen tilt in the rotor (or stator) disks produces a significant change in the air gap amplitude with respect to the design value. As a consequence, during the rotation an air gap modulation arises, and additional strengths and unbalance in the electrical quantities are expected. Similar effects arise in radial-flux machines, for instance due to the rotor eccentricity, and have been deeply investigated also with regard to PMSMs [3]-[4]. Many works concern AF machine design, and also consider mechanical features [5]-[10]; some are particularly devoted to the mechanical design [11]-[12]; but few deal with manufacturing imperfections [13]-[15]. In [11] the mechanical design and construction of a 300 kW AFPM machine is discussed; FEM simulations are used to determine the severity of the attraction force between the rotor disks. A rotor integrity design for a high- peed modular air-cored AFPM generator is performed in [12]; 2D FEM models are used to optimize the values of the parameters, then 3D FEM models are developed to verify the final design. In [13] a pure FEM-based approach (3D, both magnetostatic and transient) is adopted, with the evaluation of the air gap flux density and of the total axial force between rotor and stator; in addition, unbalanced magnetic forces and torques are calculated. In [14] a time-effective procedure to analyze the unbalanced condition is presented, based on a simplified 2D linear geometry and on the implementation of a circuit model; both the mechanical and electrical unbalancing effects are evaluated.

The design of AF machines should consider the eventuality of geometrical imperfections in order to avoid mechanical failures and the circulation of currents in the paralleled winding paths. For instance, in the first-stage mechanical design, the mechanical loads are often deduced by considering an idealized geometry without geometrical defects [16]. Such quantities can be amplified by manufacturing imperfections and it is useful to investigate their dependence on the level of the imperfection. A refined approach in the evaluation of the mechanical loads is also suitable for a more accurate estimation of the structural mass [17]-[20]. Moreover, manufacturing imperfections can produce additional losses [21]: under this point of view it is interesting to evaluate the magnitude of the circulating currents in the paralleled winding paths. Besides, time varying forces due to the air gap non-uniformity can produce a severe fatigue loading [22]. Finally, a decrease of the air gap, due to manufacturing defects, can cause a reduction of the cooling air flow through the air gap [23]. Hence, during the design, a suitable method is useful for a quick calculation of the mechanical strengths and of the circulation currents which are produced by imperfections.

Of course, FEM models are suitable to investigate such phenomena, but the parametric analysis by the FEM is heavy; analytical models are less time consuming, but the available analytical field solutions mainly refer to an idealized geometry without defects [24], [25]. In order to exploit the parametric feature of the analytical approaches, in [15] a mixed analytical-FEM method is introduced, based on the superposition of tailored "field functions". It is used to calculate the air gap flux density in an AF PMSM and the consequent no load electrical and mechanical quantities. A similar method was adopted in [26] for the analysis of a radial flux, field excited, distributed winding, synchronous machine. Each "field function" separately represents the field due to the PMs alone and to the slotting perturbations. In [15] such field functions have been identified by selective FEM analyses, even if they could also be analytically deduced [27]-[29]. In [30] the same method has been used to perform a sensitivity analysis on the effects of various kind of manufacturing imperfections in a concentrated coil AF PMSM; the considered geometrical defects were concerning the offset and the tilt of the rotor disks, and an evaluation of the resultant forces and torques on the rotor disk was carried out. However, these results have been validated only by the FEM analyses.

This paper presents the experimental measurements of the manufacturing imperfections and of some consequent operating quantities concerning a concentrated coil AF PMSM real prototype. Moreover it provides the validation

of the method and of the analysis presented in [15] and [30], by comparing the theoretical predictions and the test results concerning the prototype. Finally, some additional results concerning the stresses on the middle rotor disk and the forces on the bearings are included.

In Section II, a description of the considered concentrated coil AF-PMSM 50 kW 70 rpm prototype is provided. As aforementioned, the prototype is affected by some imperfections, due to unintentional air gap non-uniformity, which are described in Section III. Section IV resumes the method of analysis, which allows to estimate several quantities: the local stresses, the resulting forces and bending torques acting on the rotor disks, the differential electromotive forces (within parallel paths), the circulating currents in the parallel paths. Sections V provides some basic theoretical results and some evaluations concerning forces on the bearings, disk stresses and deformations at no load, and includes some results of the loaded operation. Section VI compares some theoretical and experimental results concerning the prototype and validate the method of analysis. Finally, Section VII reports the results of a sensitivity analysis concerning the effects of various kinds and grades of imperfections.

II. DESCRIPTION OF THE AF PMSM PROTOTYPE

The concentrated coil AF PMSM which is considered in this paper has been designed for the operation as a generator coupled to a wind turbine [6]. The stator winding consists of tooth concentrated coils (TCC) [31]. A machine module is shown in Fig. 1(a), the actual machine is composed by two axially adjacent modules, whose windings are displaced by 60 elec. degrees [32]. In the Fig.1(a), from left to right, the details of a coil, of a tooth and of a PM are shown. Fig. 1(b) and 1(c) show the circumferential and axial sections, and depict the main geometrical variables. The case study discussed in this paper concerns a prototype whose rated data are in Table I.

TABLE I
MAIN RATED AND CONSTRUCTION DATA OF THE PM, AXIAL FLUX, CONCENTRATED COIL MACHINE, CONSIDERED FOR THE ANALYSIS

Line-to-line rated Voltage V_n, no-load EMF E_n [V]	625, 750
Rating P_n [kW], speed N_n [rpm], frequency f_n [Hz]	50, 70, 22.17
Rated current I_n [A], eff. η [%], reactance x [pu]	46.3, 92.6, 0.50
Rated stator losses: Cu $P_{\ell cu}$, Fe P_{tfe}, [kW]	2.04, 0.39
Rated rotor losses: PM P_{tPM} [kW]	0.51
Ext. diam. D_e, int. diam. D_i, total axial length ℓ_{ax} [m]	1.1,0.914, 0.33
Rated air gap g_n, tooth axial height h_t [mm]	2.5, 97.2
Tooth head peripheral widths b_{ti}, b_{te} [mm]	21.8, 38.0
PM height h_m, radial size L_m, lat. widths b_{mi}, b_{me} [mm]	10, 93, 59, 74
No of coil turns/tooth $N_{tu.t}$, conductor sizes [mm]	83, 4×2.8
DATA OF EACH MODULE (the machine has 2 modules):	
No of teeth N_t, No of PMs/(disk side) = No of poles p	36, 38
Electro-magnetic cycles No N_c, phase No	2, 3
No of teeth/(phase·cycle) N_{tcph} = No of coil/(phase·cycle)	6

The coils of one cycle which belong to the same phase (N_{tcph} = 6 coils, see Table I) are series connected and form a phase-cycle. Fig. 2 details the distribution of the coils and of the PMs along two cycles, together with the phase-cycle sequence, while Fig. 3 shows the connections between the phase-cycles to form the phase windings [6]: capital and small letters depict the opposite direction of the coil magneto-motive forces (MMFs). Since the number of poles-

per-cycle $p_c = p/N_c = 38/2 = 19$ is odd, the second cycle is simply obtained by repeating the first cycle with exchanged small and capital letters. The two phase-cycles of the same phase are connected in parallel; this connection produces three phase-loops.
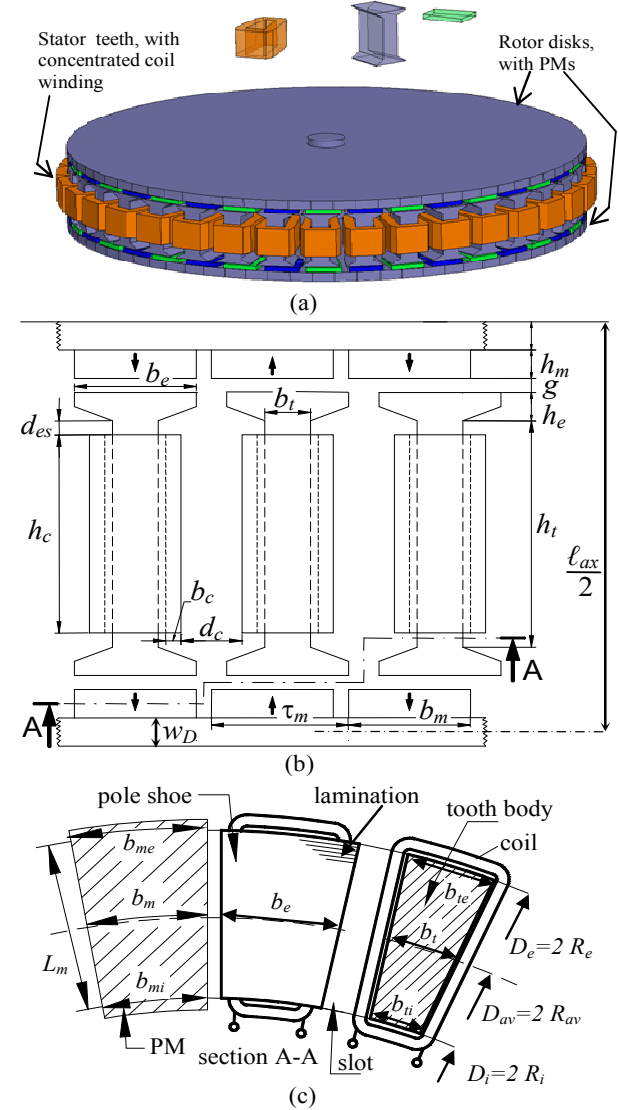

(a)

(b)

(c)

Fig. 1. Single module of an AFPM machine (a) equipped with tooth concentrated coil (TCC) windings. Machine transversal (b) and axial (c) sections and main sizes.

III. CONSIDERED GEOMETRICAL IMPERFECTIONS

Fig. 4 shows the reference frames for the analysis:
− all the angles are considered positive according to the counter clock wise direction; the same holds for the shaft rotation;
− the z axis of the stationary xyz frame overlaps the rotation axis; the x-y plane is parallel to the tooth heads surfaces; the x axis is aligned with the slot axis before a reference tooth (named tooth no. 1, t_1);
− the angular stator coordinate θ_s starts from the x axis;
− θ_r is the mechanical angle along the rotor, its origin is the axis of a reference PM (named PM no. 1, m_1, considered as a South pole);
− the rotor angular position is $\theta_{sr} = \theta_s − \theta_r$;
− all the air gap quantities are evaluated along the

circumference c_{av} shown in Fig. 4(a), that is taken as reference line: it is placed within the air gap at a distance equal $0.1 \cdot g_n$ from the teeth head surface (g_n is the rated air gap, see Table I) and in a radial position equal to half the teeth radial extension ($r = R_{av}$, Fig. 1); the abscissa w along c_{av} and the stator angular variable are each other related by $\theta_s = w/R_{av}$.

The following assumptions are invoked in the analysis:
– the no-load operation is investigated: this assumption will be discussed in Sec. V-D, comparing no-load results with results in loaded operation;
– the saturation as well as the eddy currents are neglected;
– since the modules are magnetically independent, just one module is considered;
– the rotor disks are assumed as perfectly flat and no defects are considered in the stator structure;
– the stator and the rotor shaft are coaxial.

The manufacturing imperfections taken into account by the model are the tilts and axial offsets of the two rotor disks with respect to their ideal position. In Fig. 5(a), the shaft axis of the module is horizontally disposed. By considering the ideal rotor positions without defects (dotted rectangles in Fig. 5(a)), the following quantities can be defined for the left and right PM disk (subscripts $_L$, $_R$ respectively):
– air gap p.u. offsets: g_{0Lpu}, g_{0Rpu} (g_n as a base), positive if the air gap increases;
– air gap peak amplitude, due to disk inclination: g_{1Lpu}, g_{1Rpu};
– angular position of the points with maximum air gap amplitude on the PM disk: β_L, β_R, measured from the origin of the rotor variable θ_r.

Hence, the air gap widths as a function of the rotor position θ_{sr} are given by ($q = L$ or R):

$$g_q\left(\theta_s, \theta_{sr}\right) = g_n \cdot \left(1 + g_{0qpu} + g_{1qpu} \cdot cos\left(\theta_s - \theta_{sr} - \beta_q\right)\right) \quad (1)$$

An example of the air gap modulation (in p.u.), as obtained by measurements on the prototype (see Table I), is reported in Fig. 5(b).
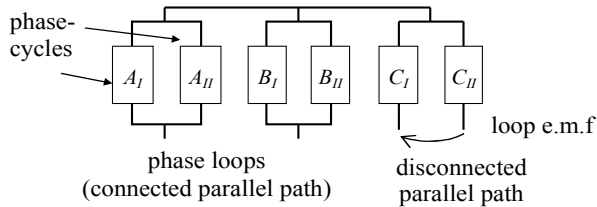

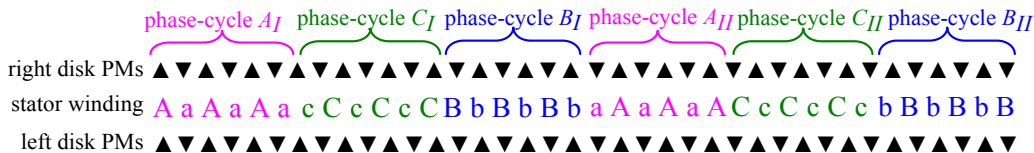Fig. 3. Connections among the phase-cycles to form the phase windings.

Fig. 4. Frames considered in the analysis (a): (x, y, z), (w, r, z). Origin of the stator and rotor angular frames (b).
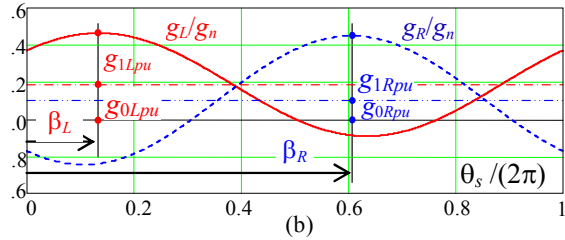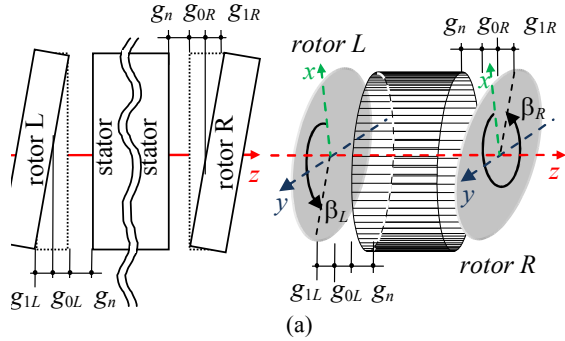
Fig. 5. Defect parameters (a) (rotor position: $\theta_{sr} = 0$). Dotted rectangles show the ideal position of the rotors (no defects). Air gap modulation (b) (in p.u.) of right and left PM disk vs θ_s (rotor position: $\theta_{sr} = 0$).

IV. ELECTRO-MECHANICAL QUANTITIES EVALUATION

All the quantities are derived from the distribution of the air gap flux density components B_w (tangential, along the circumference c_{av}) and B_z (axial). Such components are expressed as a function of the stator peripheral coordinate θ_s and of the rotor position θ_{sr} (Fig. 4). They are obtained by means of a mixed analytical-FEM approach, called "field function" approach [15]. In order to prove the effectiveness of the method, Fig. 6 shows a comparison between some flux density radial distribution results obtained by the adopted field function method and by the FEM 3D simulations.

Fig. 2. Schematic disposition of the coils (A, B, C, a, b, c) and of the PMs ($\blacktriangledown$, $\blacktriangle$) within the two cycles of one module of the machine of Table I ($N_{tcph} = 6$ teeth/(phase·cycle); $p_c = p / N_c = 19$ poles / cycle). Considering the coil senses, the two cycles form one electromagnetic cycle. The 6 coils of a phase-cycle are series connected; capital and small letters indicate the opposite directions of the coil MMFs. The winding disposition of the other machine module is the same, except for a peripheral displacement of 60 elec. degrees (corresponding to $N_{tcph} / 2 = 3$ tooth pitches [6]); this displacement also implies the systematic sense inversion of all the coils of the electromagnetic cycle belonging to the second module.
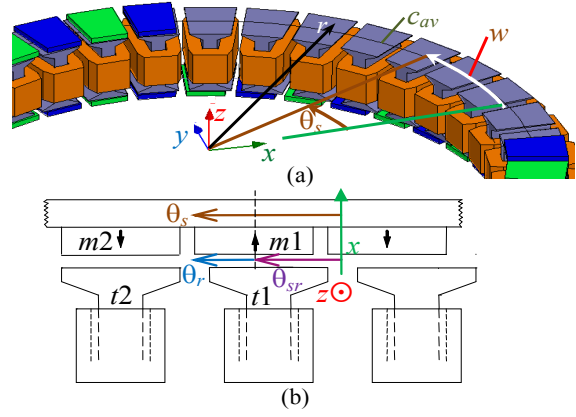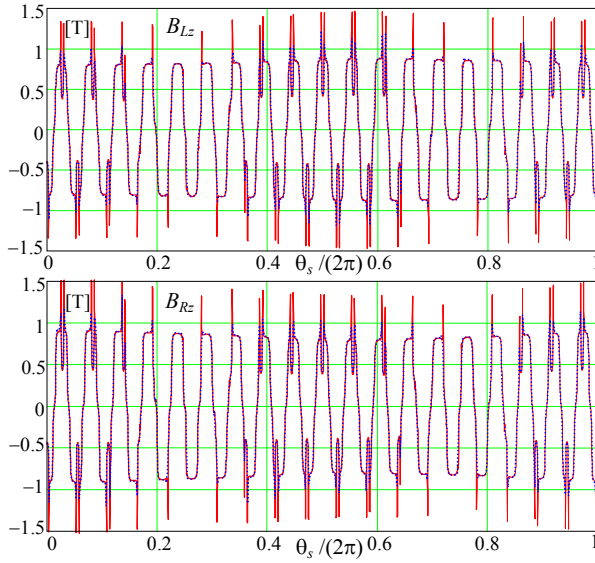
Fig. 6. The z-axis flux density distributions along the average circumference c_{av} in the left and right air gaps, for rotor position $\theta_{sr} = 0$; ⋯⋯: FEM 3D Magnetostatic analysis; ——: adopted method based on field functions.

A. Flux linkages and electro-motive forces (EMFs)

The tooth fluxes are evaluated as the surface integral of the z component of the flux density (B_{Lz} in the left air gap, B_{Rz} in the right one), within each tooth pitch τ_{tk}. The field function approach is intrinsically 2D, therefore the surface integral reduces to a line integral along the reference line c_{av}. Anyway, also the radial edge effects are taken into account, by means of a correction factor, identified by FEM ($\eta_\varphi(g_q(\theta_s, \theta_{sr}))$, see [15]).

In the analysis, the flux density is assumed positive if oriented from left to right. Thus, in the generic k-th stator tooth, an incoming flux φ_{Lk} from the left rotor disk, and an outgoing flux φ_{Rk} towards the right rotor disk are assumed, disregarding the PM orientation (Fig. 7).
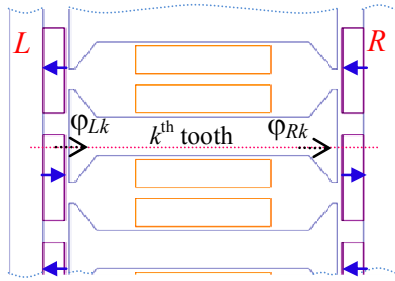

Fig. 7. Right and left magnetic fluxes in the kth tooth.

As shown in Fig. 7, the coils are symmetrical with respect to the teeth axes: this fact determines the symmetry of the inter-tooth field lines between adjacent teeth. Thus, the no-load flux linkage ψ_{tk} of the k-th tooth-coil, with $N_{tu.t}$ turns, is simply given by:

$$\psi_{tk}\left(\theta_{sr}\right) = N_{tu.t} \cdot \left(\varphi_{Lk}\left(\theta_{sr}\right) + \varphi_{Rk}\left(\theta_{sr}\right)\right)\big/ 2 \quad . \quad (2)$$

In order to calculate the no-load phase flux linkages, the winding structure has to be considered. The N_{tcph} coils of one phase-cycle are series connected: as shown in Fig. 2, where N_{tcph} = 6, the MMFs of adjacent coils have opposite direction. Assuming h = 0, 1, 2, 3, 4, 5 for the phase-cycles $pc = A_I, C_I, B_I, A_{II}, C_{II}, B_{II}$ respectively, their no-load flux linkages $\psi_{pc} = \psi_{pc}(\theta_{sr})$ are given by:

$$\psi_{pc}\left(\theta_{sr}\right) = \left(-1\right)^h \cdot \sum_{k=h\cdot N_{tcph}+1}^{(h+1)\cdot N_{tcph}} \left(-1\right)^k \cdot \psi_{tk}\left(\theta_{sr}\right) \quad . \quad (3)$$

Clearly, in the case of perfect machine, the 2 phase-cycles of the same phase (which form a phase loop, Fig. 3) have identical flux linkage; on the contrary, in the case of defects, the following differential flux linkages act in the phase loops:

$$\begin{aligned}\psi_{dA}\left(\theta_{sr}\right) &= \psi_{AI}\left(\theta_{sr}\right) - \psi_{AII}\left(\theta_{sr}\right)\\ \psi_{dB}\left(\theta_{sr}\right) &= \psi_{BI}\left(\theta_{sr}\right) - \psi_{BII}\left(\theta_{sr}\right) \quad . \quad (4)\\ \psi_{dC}\left(\theta_{sr}\right) &= \psi_{CI}\left(\theta_{sr}\right) - \psi_{CII}\left(\theta_{sr}\right)\end{aligned}$$

By time deriving (4), the no-load loop EMFs follow:

$$e_\ell\left(t\right) = \frac{d\psi_\ell\left(\theta_{sr}\left(t\right)\right)}{dt} = \frac{d\psi_\ell\left(\theta_{sr}\right)}{d\theta_{sr}} \cdot \frac{d\theta_{sr}}{dt} = \frac{d\psi_\ell\left(\theta_{sr}\right)}{d\theta_{sr}}\Omega \quad , \quad (5)$$

with $\ell = dA$, dB or dC, and where Ω is the angular mechanical speed.

B. Loop Parameters and Currents

The loop EMFs (5) cause the circulation of currents in the phase loops. In order to evaluate these currents, the loop parameters (resistance and inductance) are needed.

Some preliminary magnetostatic FEM simulations (with passive PMs: zero remanence B_r, PM permeability μ_{rev}) show that the mutual inductances between loops of different phases are very low. Therefore, each loop current can be evaluated on the basis of the self-inductance of the loop itself. Such inductance L_{loop} follows from the system energy W_m, with just one current I_{loop} acting: $L_{loop} = 2W_m/I_{loop}^2$. The result is: L_{loop} = 70.6 mH.

The loop resistance R_{loop} is evaluated on the basis of the geometrical coil dimensions (R_{loop} = 0.64 Ω).

The loop current waveforms of each phase loop can be evaluated by means of the loop voltage laws:

$$L_{loop}\, di_{loop.ph}\big/dt + R_{loop}i_{loop.ph} = e_{d.ph}\left(t\right) \quad , \quad ph = \text{A, B, C} \, . \quad (6)$$

C. Stress distribution in the air gap

Both the resultant axial forces and tilt torques which act on the rotor disks are practically due only to the stress component σ_z parallel to the rotation axis. Thus, only this component is considered. In the x,y,z reference frame, σ_z is deduced from the Maxwell stress tensor in the air gap:

$$\sigma_z = \frac{B_z^2\left(x,y,\theta_{sr}\right) - \left(B_x^2\left(x,y,\theta_{sr}\right) + B_y^2\left(x,y,\theta_{sr}\right)\right)}{2\cdot\mu_0} \quad . \quad (7)$$

Moving to polar coordinates r,θ_s,z, the following holds:

$$B_x^2 + B_y^2 = B_r^2 + B_w^2 \quad . \quad (8)$$

Along the circumference c_{av} (Fig. 4(b)) the radial component B_r is negligible; thus:

$$\sigma_{qz}\left(\theta_{s},\theta_{sr}\right)=\left(B_{qz}^{2}\left(\theta_{s},\theta_{sr}\right)-B_{qw}^{2}\left(\theta_{s},\theta_{sr}\right)\right)\Big/\left(2\mu_{0}\right); \quad (9)$$

where the sub-script $q = R, L$ refers to the right and to the left disk.

D. Axial Forces

The axial force which acts on a rotor disk (and on one side of the stator) is evaluated by integrating σ_z over the air gap area A_g (parallel to the x, y plane) midway between rotor PMs and stator tooth heads. Similar to the fluxes, due to the 2D formulation, this surface integral reduces to a line integral along the circumference c_{av} , times the radial dimension L_m :

$$F_{q}\left(\theta_{sr}\right)=\int_{0}^{2\pi}\sigma_{qz}\left(\theta_{s},\theta_{sr}\right)\cdot\eta_{\sigma}\left(g_{q}\left(\theta_{s},\theta_{sr}\right)\right)\cdot R_{av}\cdot L_{m}d\theta_{s} . (10)$$

In (10), the $\eta_{\sigma}(g_{q}(\theta_{s},\theta_{sr}))$ is the FEM identified correction factor, which allows to take into account the radial fringing edge effects in the evaluation of the force integral quantities: the details of its evaluation are given in [15].
The resultant force acting on the stator is the difference between F_R and F_L :

$$F_{stat}\left(\theta_{sr}\right)=F_{R}\left(\theta_{sr}\right)-F_{L}\left(\theta_{sr}\right) \quad . \quad (11)$$

E. Bending Torques on the Rotor Disks

The resultant bending torque T is obtained by composing the x and y components T_x and T_y due to the disk tilts:

$$T_{qx}\left(\theta_{sr}\right)=L_{m}R_{av}^{2}\int_{0}^{2\pi}\sigma_{qz}\left(\theta_{s},\theta_{sr}\right)\cdot\eta_{\sigma}\left(g_{q}\left(\theta_{s},\theta_{sr}\right)\right)\cdot sin\left(\theta_{s}\right)d\theta_{s}$$
$$T_{qy}\left(\theta_{sr}\right)=L_{m}R_{av}^{2}\int_{0}^{2\pi}\sigma_{qz}\left(\theta_{s},\theta_{sr}\right)\cdot\eta_{\sigma}\left(g_{q}\left(\theta_{s},\theta_{sr}\right)\right)\cdot cos\left(\theta_{s}\right)d\theta_{s}$$
$$, \quad (12)$$

$$T_{q}\left(\theta_{sr}\right)=\sqrt{T_{qx}^{2}\left(\theta_{sr}\right)+T_{qy}^{2}\left(\theta_{sr}\right)} \quad , \qquad q=R,L . \quad (13)$$

V. THEORETICAL PREDICTIONS ON THE PROTOTYPE

A. Basic results

Figs. 8-12 show the distribution of the electrical and mechanical quantities evaluated by means of the adopted method, in the case of the defect parameters of Table II (obtained from measurements on the prototype of Table I, see Section VI). All the time waveforms refer to one complete rotor revolution at rated speed, while the spatial distribution in Fig. 10 refers to the rotor position $\theta_{sr} = 0$.
Fig. 12 shows that the disk tilts produce a resultant bending torque, the peak to peak ripple of which is about 0.25 times the average value. Such a ripple induces a pulsating fatigue loading on the disks and on the shaft. Thus, the torque calculated by the adopted method can be effectively used in a structural analysis routine in order to verify the safety with respect to mechanical failure due to the fatigue.

TABLE II
IMPERFECTION PARAMETERS ACCORDING TO (1),
ADOPTED FOR THE ANALYSIS OF THE MACHINE OF TABLE I.

Disk	g_{0pu}	g_{1pu}	β [°]
Left	0.187	0.278	48.2
Right	0.102	0.348	217.9

As shown, the adopted analytical method is 2D, because

all the field evaluations are carried out along the circumference placed at half the teeth radial extension.
However, thanks to the corrective factors $\eta_{\varphi}(g_{q}(\theta_{s}, \theta_{sr}))$ and $\eta_{\sigma}(g_{q}(\theta_{s}, \theta_{sr}))$, which take into account the radial fringing edge effects, the predicted integral quantities are in very good agreement with the 3D FEM results [15].
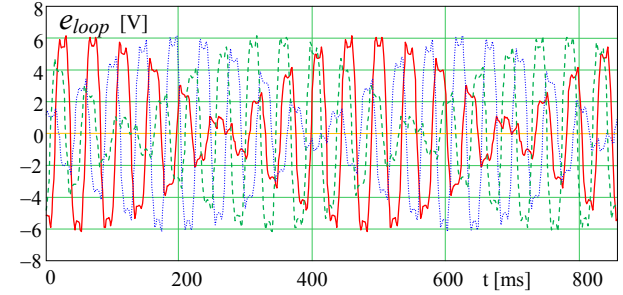
Fig. 8. Waveforms of the loop EMFs (by (5)) of the three phases during one complete rotor revolution at rated speed.
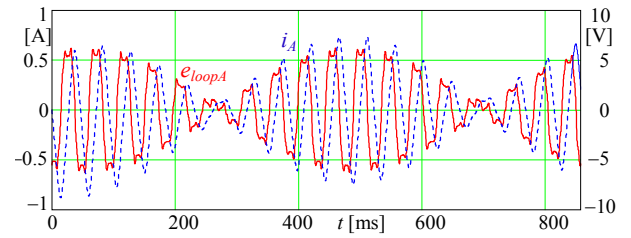
Fig. 9. Waveforms of the loop EMF (by (5)) and of the loop current (by (6)) of phase A, during one complete rotor revolution at rated speed.
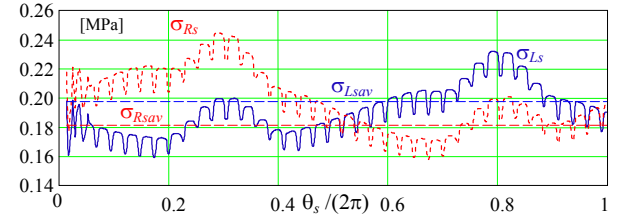
Fig. 10. Smoothed distributions of the z-axis stress $\sigma_{Lz}(\theta_s)$ and $\sigma_{Rz}(\theta_s)$ in the left and right air gaps, along the circumference c_{av}, evaluated by (9), for the rotor position $\theta_{sr} = 0$. A moving average has been applied, extended to the points within 2 tooth pitches; constant dotted lines: left $\sigma_{Lz.av}$ and right $\sigma_{Rz.av}$ average stress values.
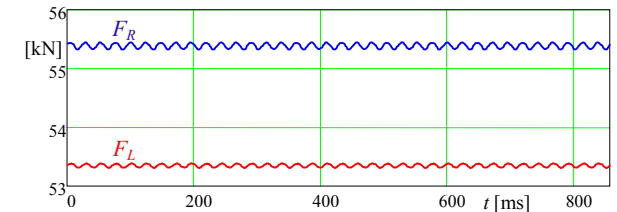
Fig. 11. Waveforms of the axial forces on the left and the right PM disks (by (10)), during one complete rotor revolution at rated speed.
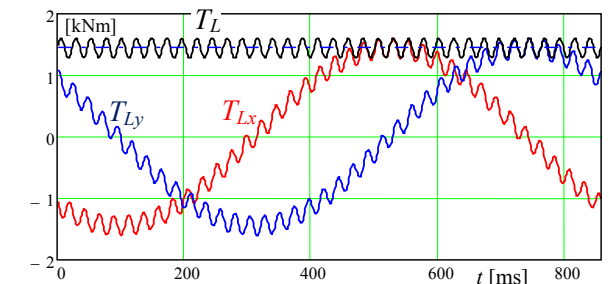
Fig. 12. Waveforms of the bending torque on the left PM disk: x and y

components T_{Lx} , T_{Ly} (by (12)) and resultant T_L (by (13)). The bending torques on the right PM disk are similar. The ripple in the resultant torque T_L produces fatigue loading in the shaft.

B. Incremental resulting forces on the bearings.

Under ideal conditions, without any imperfection, the generator bearings are loaded with the forces due to the wind turbine actions, to the bearing preloads and to the rotor weight. As a consequence of the imperfections, additional forces acting on the bearings are expected: such incremental forces can be calculated by using the resulting torques on the disks. For this purpose, the shaft shown in Fig. 13 can be modeled as a hinged beam, whose constraints are placed in line with the tapered roller bearings. Since the machine consists of two modules, also the resulting tilt torques and axial forces due to the geometrical defects (air gap modulations, see Fig. 16) in the second module have been evaluated (i.e. T_{L2} , T_{R2}).
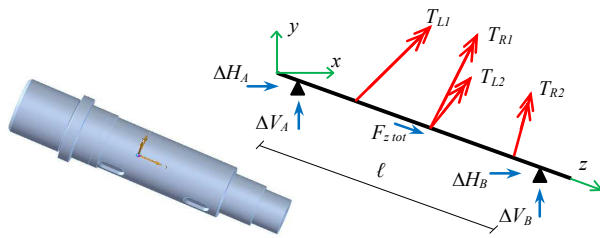

Fig. 13. Actual shaft structure and corresponding beam model to find the resulting incremental constraint forces acting on the shaft, due to the geometrical manufacturing defects.

The flexional behavior of the beam in Fig. 13 is statically determined, so that the incremental forces ΔH_A , ΔV_A , ΔH_B , ΔV_B acting on the shaft (equal and opposite to those acting on the bearings) follow from the equilibrium equations:

$$\Delta H_A = \frac{1}{\ell}\left(T_{L1y} + T_{R1y} + T_{L2y} + T_{R2y}\right) \ , \ \Delta H_B = -\Delta H_A$$

$$\Delta V_A = -\frac{1}{\ell}\left(T_{L1x} + T_{R1x} + T_{L2x} + T_{R2x}\right) \ , \ \Delta V_B = -\Delta V_A$$

(14)

The waveforms of ΔH_B and ΔV_B during one rotor revolution are shown in Fig. 14: similarly to the tilt torques they are almost sinusoidal and exhibit a certain ripple.

The axial forces on the bearings due to the axial force $F_{z.tot}$ depend on the stiffness of the whole system and on the bearing preload, and thus require a more refined approach.
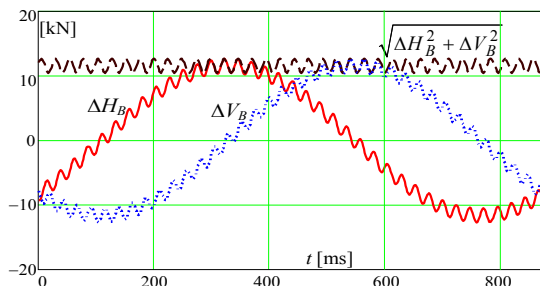

Fig. 14. Waveforms of the incremental forces on the right bearing (B).

C. Strain and stress distribution on the central disk

The air gap stress (9) also causes bending effects on the disks, which can be analyzed by analytical or FEM models. Under this point of view, the condition of the central rotor disk (see Fig. 17) is the most critical, because, unlike the external disks, it cannot be reinforced by ribs.

Fig. 15 shows the displacements and the Von Mises stress distribution on the surface of the central disk. They have been obtained by a static linear FEM analysis performed by Comsol Multiphysics® v.4.2. The PMs have been neglected and the disk has been modeled by tetrahedral elements.

All the rotor disks are fixed on a common drum, which is mounted on the shaft. Due to this, the nodes of the internal surface of the disk hole shown in Fig. 15 have been considered as fixed. The disk surfaces have been loaded by the pressure distributions (9), which have been calculated on the actual machine by the aforementioned procedure. The maximum Von Mises stress (about 21 MPa) occurs near the hole and is considerably lower than the yielding stress. The displacement of the disk is practically dominated by the first harmonic in the air gap stress distribution (9), which is due to the modulation of the air gap amplitudes. Moreover the maximum axial displacement is about 0.14 mm.
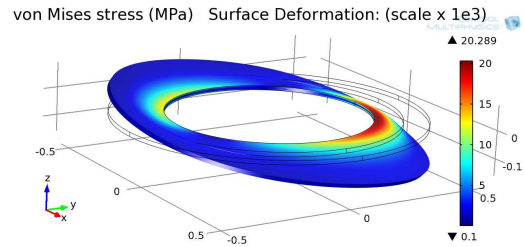

Fig. 15. Von Mises stress [MPa] on the external surface of the central rotor disk and axial displacements (amplified by 10^3).

D. Remarks on the operation under load

For completeness, also the behavior under the rated load has been analyzed. For this purpose, some 3D FEM transient simulations have been performed (Ansys Maxwell® v.16), by considering only one module alone and using sinusoidal line currents as sources. According to the maximum torque-per-ampere control strategy, the stator MMF has been set in quadrature with the PM MMF. The results are reported in Table III: they show that, with respect to the no load operation, little differences in the values of the resultant tilt torques and axial forces on the disks occur. Moreover, the currents in the paralleled paths of each phase practically equal each other: their differences are comparable to the magnitude of the loop circulating currents at no load. Thanks to this rather balanced sharing, further operating conditions have been investigated by some 3D FEM magnetostatic analyses, by setting identical three-phase systems of currents in the two parallel winding paths. Three different operating conditions have been considered, all at rated current: purely magnetizing stator MMF, in quadrature MMF, purely de-magnetizing MMF. The results are reported in Table IV. Also Table IV confirms that, compared to the no-load operation, the stator in-quadrature MMF produces a minimal change to the resultant forces and torques on the disks (+2% in the forces, -5% in the torques). Besides, a de-magnetizing MMF reduces the resultant forces and torques.

The discrepancies between torque values in the transient and the magnetostatic simulation results (bold lines in Tables III and IV) are due to the high ripple (Fig. 12) and to the different presented results: the transient torques have

been time averaged along a revolution, whereas the magnetostatic torques refer to the position $\theta_{sr} = 0$.

These results lead to conclude that, when the stator MMF is mainly in-quadrature with respect to the PM MMF, the change in the resultant forces and torques is small. Thus, just a minimal variation in the strain distribution should be induced with respect to the no-load operation. Therefore, even if the analysis at no load is used, a fair evaluation of the forces and torques on the disks can be obtained.

TABLE III
COMPARISON OF AVERAGE FORCES AND TORQUES BETWEEN NO-LOAD AND LOAD OPERATION (3D TRANSIENT FEM SIMULATIONS)

Absolute forces and torques	F_L kN	F_R kN	T_L kNm	T_R kNm
No-load	53.75	55.95	1.49	2.06
Load (in quadrature MMF)	54.95	57.07	1.54	2.07
Ratio load/no-load	**1.02**	**1.02**	**1.04**	**1.00**

TABLE IV
COMPARISON OF FORCES AND TORQUES BETWEEN NO-LOAD AND LOAD OPERATION (3D MAGNETOSTATIC FEM SIMUL., IN THE POSITION $\theta_{SR} = 0$)

Absolute forces and torques		F_L kN	F_R kN	T_L kNm	T_R kNm
No-load		53.89	55.89	1.44	2.02
Load	magnetizing MMF	64.81	67.05	1.61	2.28
	in quadrature MMF	54.76	56.78	1.36	1.93
	demagnetizing MMF	44.76	46.49	1.28	1.67
p.u. changes, with respect to no-load					
magnetizing MMF		1.20	1.20	1.12	1.13
in quadrature MMF		**1.02**	**1.02**	**0.95**	**0.95**
demagnetizing MMF		0.83	0.83	0.89	0.82

VI. EXPERIMENTAL RESULTS

In order to validate experimentally the method, some measurements have been carried out on the prototype, which is characterized by some level of imperfection, due to the manufacturing process. In particular, the tests regard some electrical quantities (loop EMFs, currents). No mechanical quantities (stresses and bending torques) have been experimentally measured, due to practical difficulties. In fact, the bending torques should be reconstructed starting from some strain measurements on the disk surfaces. This procedure would require several strain gauges, as well as a reconstruction algorithm which deduces the stress tensor in the disk thickness and operates proper integration of the stress components to find the resulting torques. Without an accurate tuning, such an approach might provide misleading results, due to the thermal drift in the strain gauges and to the uncertainties in the structural model as well as in the material parameters. Finally, the strain gauge signals would be strongly disturbed, because of the harsh electromagnetic environment inside the machine.

Nevertheless, the mechanical quantities are a direct consequence of the magnetic field, which is also the cause of the loop EMFs and of the circulating currents. Thus, the good agreement between model and test results related to the electrical quantities provides an indirect validation of the results concerning the mechanical quantities.

Fig. 1 shows only one machine module (with two air gaps), however the actual machine of Table I, shown in Fig. 16(a), has two modules (thus there are four air gaps). For the details of the prototype and of the experimental setup see [6] and [32].

First of all, the clearance in the four air gaps has been measured; the measure is performed in front of two chosen, axially aligned teeth, during a complete revolution. Fig. 17 shows the measured values in the four air gaps a,b,c,d (indicated by △, □, ◇, ○), for N_{rp} = 38 rotor positions. The figure shows also the sinusoidal data fitting, according to (1). The p.u. rms error in the xth air gap width is

$$\varepsilon_x = \frac{1}{g_{1x}} \cdot \sqrt{\frac{1}{N_{rp}} \cdot \sum_{k=1}^{N_{rp}} \left(g_{x.meas.k} - g_{x sinus}(\theta_k)\right)^2} \quad ; \quad (15)$$

the related values are: $\varepsilon_a = 0.085$; $\varepsilon_b = 0.063$; $\varepsilon_c = 0.078$; $\varepsilon_d = 0.185$. The assumption of sinusoidal fitting functions appears justified, especially for the air gaps a and b, that exhibit the lowest ε values. The air gaps a and b in Fig. 17 belong to the first module and coincide with the air gaps L and R respectively (see Fig. 5).
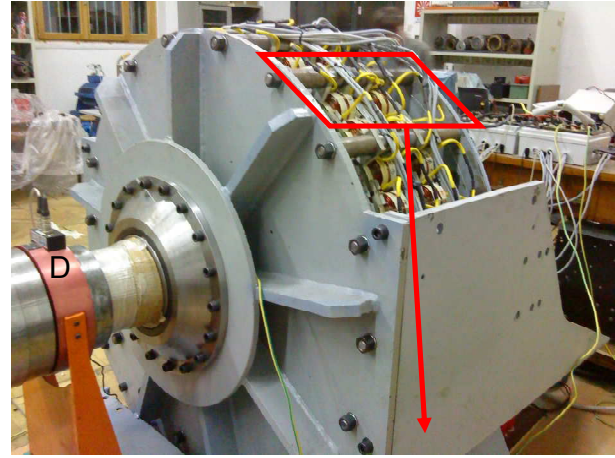
(a)
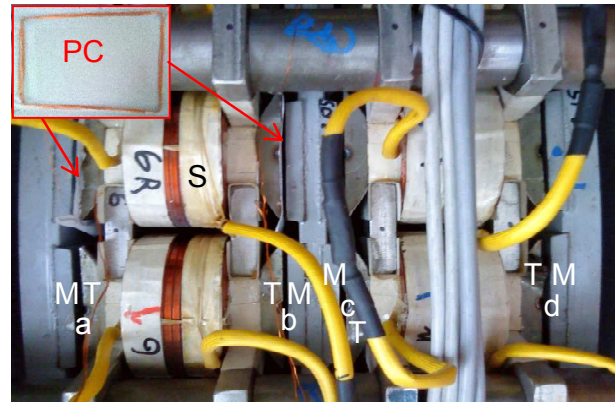
(b)

Fig. 16. Prototype used in the laboratory tests, characterized by some geometrical imperfections (offsets and tilts of the rotor disks, as shown in Table I and Fig 17). (a) global view (D = torque-meter); (b) zoom of the red parallelogram, with the actual position of two coils at the two heads of one tooth; PC in the top left angle shows one probe coil before the introduction in the air gap; M = PMs, T = tooth heads, a, b, c, d = air gaps; SC = stator winding coil.

Due to the imperfections, the incoming flux φ_{Lk} and the outgoing flux φ_{Rk} in one tooth are different from each other (see Fig. 7). To verify this effect, two probe coils have been prepared (PC in Fig. 16(b), top-left), and inserted in the air gaps, each one in front of the tooth heads.
Fig. 18(a) shows the measured EMFs in the prototype and Fig. 18(b) the simulated ones (obtained by time derivation of

the tooth flux expressions φ_{Lk} , φ_{Rk} , see (2)): the congruence is good, both in the waveform shape, and in the amplitudes.

Afterwards, again in the no-load operation, the loop EMFs have been measured (Fig. 3, in case of disconnected parallel paths). Fig. 19 shows the open parallel loop EMF waveforms of the three phases during one complete rotor revolution at rated speed.
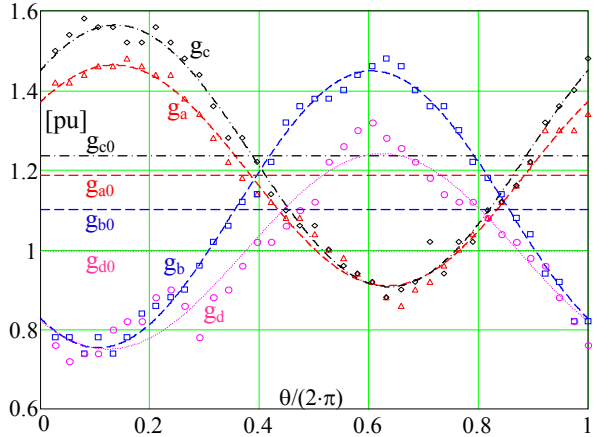

Fig. 17. Measured air gap p.u. widths (g$_a$ = △, g$_b$ = □, g$_c$ = ◇, g$_d$ = ○, measured as a function of the rotor position), their average offset values (g$_{a0}$, g$_{b0}$, g$_{c0}$, g$_{d0}$, to be considered starting from the value 1) and their sinusoidal fittings, in the four air gaps of the prototype (g$_{ref}$ = g$_n$).
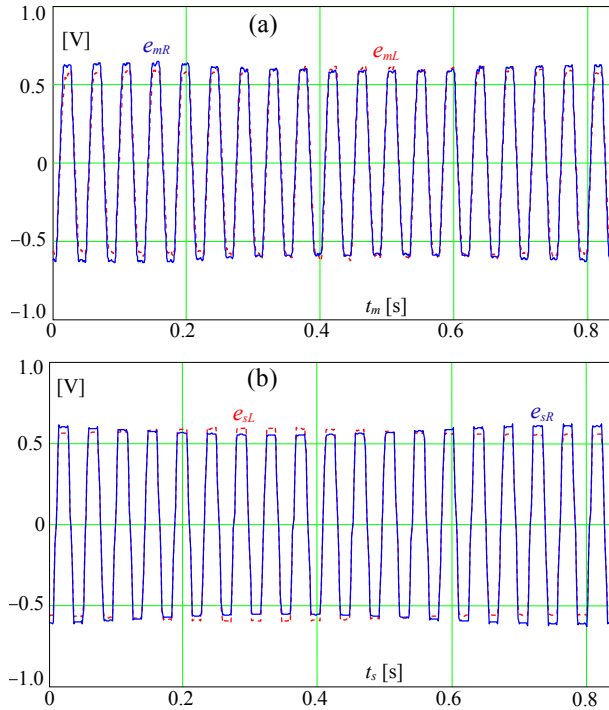

Fig. 18. Waveforms of the measured (e_m, (a)) and analytically simulated (e_s, (b)) EMFs in the two probe coils of Fig. 17, in the no-load operation (N.B.: the two time variables, t_m and t_s, do not have the same origin).
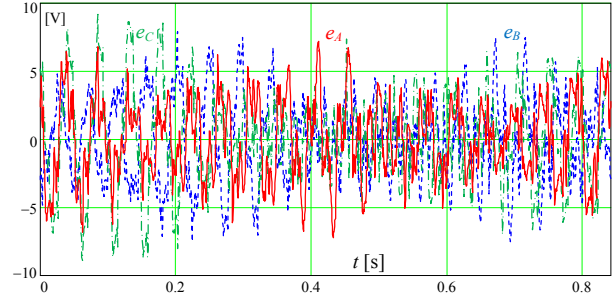

Fig. 19. Loop EMFs during one complete rotor revolution at rated speed, in the no-load operation: measured waveforms in the 3 phases.

As it can be observed, the loop EMFs are very noisy, and the three waveforms are not equal to each other: this indicates some stator manufacturing defects which are mainly due to axial displacements among teeth. Such stator non ideality is not taken into account in our model, where the stator is assumed as perfect (see assumptions in Sec. II), thus in the model the EMFs appear equal in the three phases (Fig. 8). Anyway, the general comparison with the evaluated waveforms shows a fair agreement in the case of amplitudes and envelope shape. This is better highlighted in Fig. 20, which shows the direct comparison between the measured and the simulated loop EMF for phase A, again during one complete rotor revolution at rated speed. The local differences in the waveforms are due to the cited stator non ideality, here not modeled. The corresponding r.m.s. values are E_s = 3.56 V (simulated, equal for all phases) and E_{mA} = 2.78 V, E_{mB} = 3.41 V, E_{mC} = 4.09 V, with an average value of E_m = 3.43 V, thus the ratio between the simulated and the averaged measured value is 3.56/3.41 = 1.04.
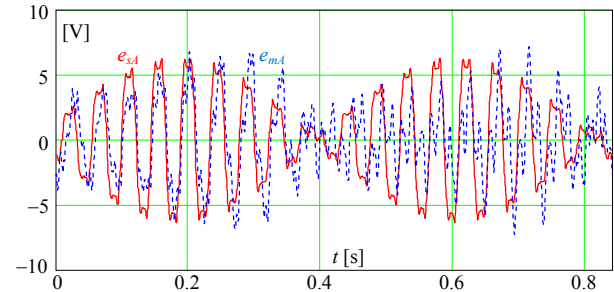

Fig. 20. Loop EMFs during one complete rotor revolution at rated speed, in the no-load operation: comparison between the measured (e_{mA}) and the simulated (e_{sA}) loop EMF of phase A.

In a similar manner, in the no-load operation, the loop currents have been measured (Fig. 3, in case of all connected parallel paths). Fig. 21(a) shows the waveforms of the 3 loop currents during one complete rotor revolution at rated speed, and Fig. 21(b) shows the direct comparison between measured and evaluated loop currents in phase A. Similar remarks like those of Figs. 19-20 hold.

The machine parameters (resistances and inductances reported in Table I) have been analytically evaluated. As a validation, the phase loop differential equation (6) has been applied, by using the measured loop EMF as an input (such EMF takes into account all the manufacturing defects): the evaluated current i_{smA} has been compared with the measured loop current i_{mA}. Fig. 22 shows such a comparison: this time, the agreement is better, confirming the correctness of the loop parameter evaluation.

Finally, the model predicts that, above 30-40% of the rated speed, the rms loop current is nearly independent of

speed, since the resistance can be neglected compared to the inductive reactance; being $E = \omega \cdot \psi$, it follows:

$$I_{loop} = \frac{E}{\omega L_{loop} \cdot \sqrt{1 + \left[R_{loop} \big/ \left(\omega L_{loop} \right) \right]^2}} \approx \frac{\psi}{L_{loop}} . \qquad (16)$$

In order to verify this effect, the loop currents at different speed have been measured. Fig. 23 shows the theoretical behavior of the loop current (r.m.s. value) as the speed increases, and the measured points (average value of the three phases): the agreement is good.
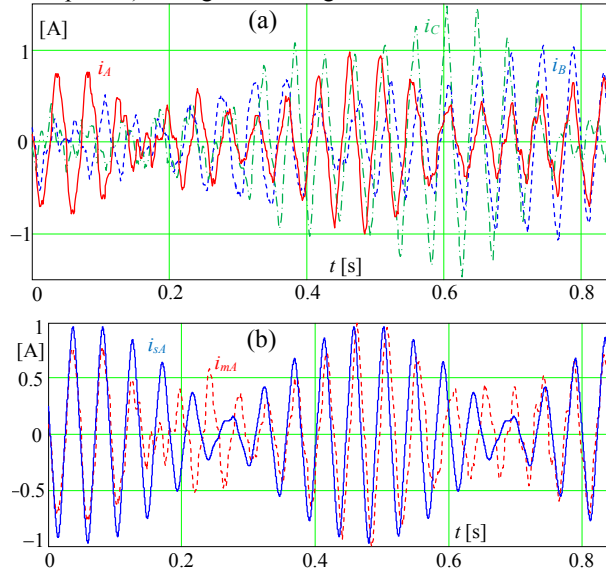

Fig. 21. Loop currents during one complete rotor revolution at rated speed, in the no-load operation. Measured waveforms (a) in the 3 phases. comparison (b) between the measured and the simulated loop current of phase A.
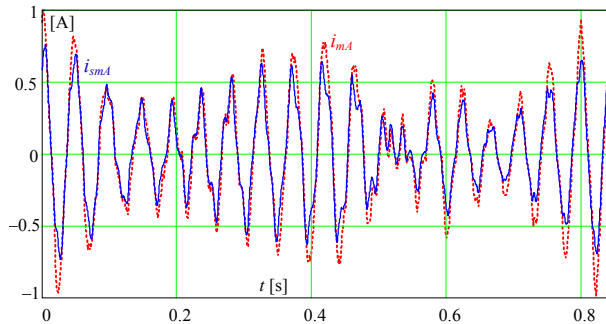

Fig. 22. Loop currents during one complete rotor revolution at rated speed, in the no-load operation. Comparison between the measured current (i_{mA}), and the current (i_{smA}) evaluated by putting the measured EMF in eq. (6).
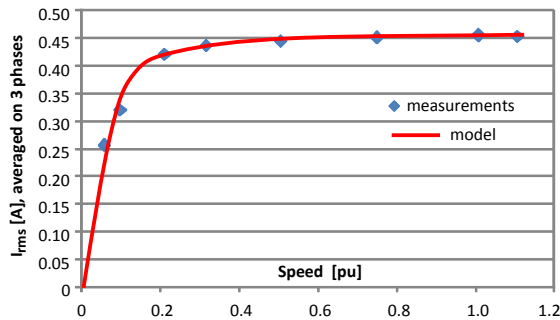

Fig. 23. Theoretical behavior of the loop current I_{rms_loop} (r.m.s. value) as the speed increases, and some measured points.

VII. SENSITIVITY STUDY OF SOME IMPERFECTION CASES

Now, in order to selectively analyze the sensitivity to each effect, just one imperfection type is regarded at a time, by considering some specific offsets and tilts on the disks, and by evaluating their consequences. In addition to the symmetrical situation (case 0), other seven cases are analyzed, with the dispositions sketched in Fig. 24 and resumed in Table V (see Fig. 5(a) and Fig. 16 too).

For every case, four imperfection values are regarded: the quantities g_0 and g_1 equal 0.2, 0.4, 0.6, 0.8 p.u., and the considered values of β are 70, 140, 210, 280 deg (mech.).

The outcomes of the study are illustrated in Fig. 25-28, in which several p.u. variables are presented as a function of the p.u. displacements (g_0 or g_1) or of the angle β:
– the rms value of the loop EMFs and of the loop currents (E_{rms_loop} , I_{rms_loop}), averaged on the three phases, at nominal speed; the reference values V_{ref} , I_{ref} are the nominal voltage of one phase-cycle ($0.5 \cdot V_n/\sqrt{3} = 180.4$ V, since the machine has two series connected modules) and the rated current in each phase-cycle ($0.5 \cdot I_n = 23.15$ A, since each phase winding consists of two parallel paths);
– the average value of the forces on the left and right disks (F_{L_av} , F_{R_av}), by (10), and their difference (F_{stat_av}), by (11), that corresponds to the global force applied to the stator; the reference value F_{ref} equals the force applied to each disk in the case of defects absence (57.87 kN);
– the average value of the bending torques applied to the left and right disks (T_{L_av} , T_{R_av}), by (13); the reference value T_{ref} equals the force reference value times the mean radius ($F_{ref} \cdot R_{av}$ = 58.28 kNm).

The most important comments are given below.

TABLE V
IMPERFECTION PARAMETERS FOR EACH STUDIED CASE

case	g_{0L}	g_{0R}	g_{1L}	g_{1R}	β_L	β_R
0	0	0	0	0	0	0
1	g_0	$- g_0$	0	0	0	0
2	g_0	0	0	0	0	0
3	0	0	g_1	0	0	0
4	0	0	g_1	$- g_1$	0	0
5	0	0	g_1	g_1	0	0
6	0	0	0.2	0.2	β	0
7	0	0	0.8	0.8	β	0

Machine with no imperfections (case 0)

As expected, neither loop EMFs (and consequent loop currents), nor bending torques take place; the forces on the disks are balanced ($F_{L\_av} = F_{R\_av} = F_{ref}$). It should be noticed that, in the combination 36 teeth – 38 poles, the squared axial flux density exhibits two periods along the circumference. Thus, the two lobes of the air gap axial stress distribution originate two opposite bending torques on each half-disk, globally cancelling each other. Of course, the two pressure lobes produce local bending with more serious effects in the case of low periodicity.

Offsets only (cases 1 and 2, Fig. 25)

Also in this case no loop EMFs and corresponding currents and no bending torques exist. The forces on the two disks F_{L_av} , F_{R_av} are unlike, and the higher value occurs in the lower air gap. The global axial force on the stator F_{stat_av}

raises with the offset growth, and is roughly proportional to the offset. The force is higher in the case of both the air gaps with offset (case 1): in this condition, F_{stat_av} can achieve significant levels, similar to the force applied on one disk without imperfections ($F_{ref} = 57.87$ kN). Again in the case 1, it outcomes F_{stat_av} [pu] $\approx g_0$ [pu]: thus, the pu function $F_{stat\_av}(g_0)$ is a straight line, whose slope roughly equals 1.

Rotor disk tilts only (cases 3, 4, 5, Fig. 26)

The loop EMFs equal zero in the case of equal tilts (case 4), and they grow with the tilts in the cases 3 and 5; however, they are rather small, thus also the corresponding currents and losses can be normally considered acceptable, unless with very great level of imperfection. In particular, in case 5, if $g_1 = 0.8$, E_{rms_loop} and I_{rms_loop} equal 0.355 and 0.28 respectively.

In cases 4 and 5, the forces on the two disks are roughly the same ($F_{L\_av} \approx F_{R\_av}$); furthermore, they are close to the values without imperfections (compared with the no imperfections condition, the maximum raise equals 6% roughly, in case 5); as a consequence, the global axial force on the stator F_{stat_av} is zero or negligible.

As concerns the bending torques, if just one tilt occurs (case 3), the torque originates practically just on the tilted disk; in the cases 4 and 5, the bending torques acting on the two disks have the same value. Nevertheless, case 5 is more critical, as concerns both the failure danger and the disk-stator contact occurrence. In fact, it can be proven that, in a shaft with uniform flexional stiffness, the bending torque system of the case 5 causes a rotation of the shaft end sections which is roughly three times the one of the case 4. Finally, the torques are proportional to the tilt g_1, as clearly evidenced in Fig. 27.

Phase displacement between the tilts (angle $\beta_L \neq 0$, cases 6 and 7, Fig. 28).

The behavior is roughly the same of the cases with $\beta_L = 0$. While EMFs and torques appear feebly dependent on the phase shift β_L, they depend on the tilt magnitude (g_1): in fact, the maximum values of E_{rms_loop}, I_{rms_loop}, T_{L_av}, T_{R_av} of cases 6 and 7 are quite close to the maximum values of case 5, for the same defects amplitude (i.e.: compare case 5 (for $g_1 = 0.2$) with case 6, and case 5 (for $g_1 = 0.8$) with case 7).

It is worth noticing that the machine defect characteristics not only can be imputed to manufacture imperfections of specific parts or to element mounting inaccuracies. They are also induced by the mechanical strains accompanying the initial assembling imperfections. With the aim to estimate the actual defects conditions, an iterative procedure could be carried out, as usually made in the study of structures with geometrical nonlinearity. At each iteration the local air gap width is updated until convergence, by considering the strains due to the strengths estimated at the previous step. In this regard, the displacements supposed in the study are those measured on a prototype. Thus, they are the "final" displacements which would result from the referred iterative process, starting from some initial fabrication or mounting imperfections.
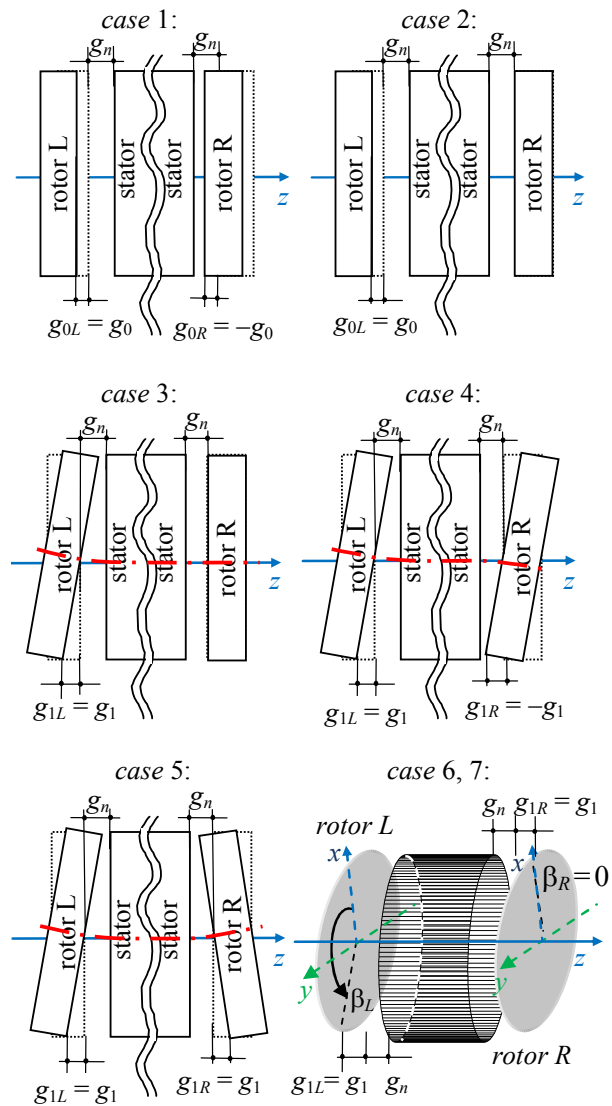

Fig. 24. Graphic illustration of the cases described in Table V. In cases 3, 4, 5 the dotted-dashed line represents the inflected axis of the shaft.
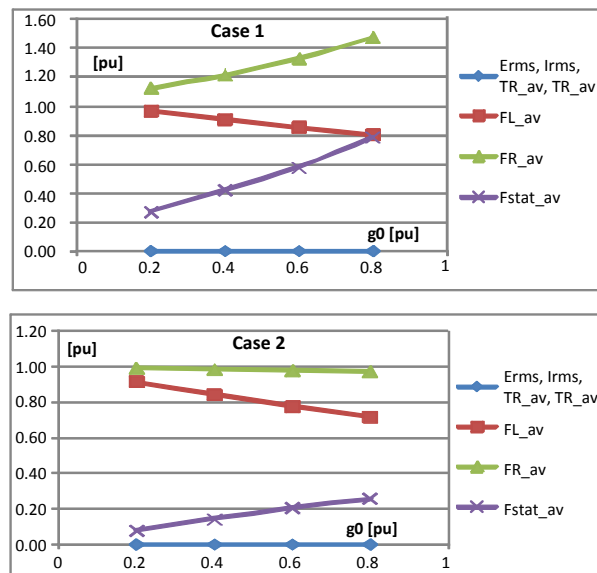

Fig. 25. Evaluated quantities, as a function of offset g_0, in cases 1 and 2. In case 1, the slope of the average p.u. force F_{stat_av} is about 1.
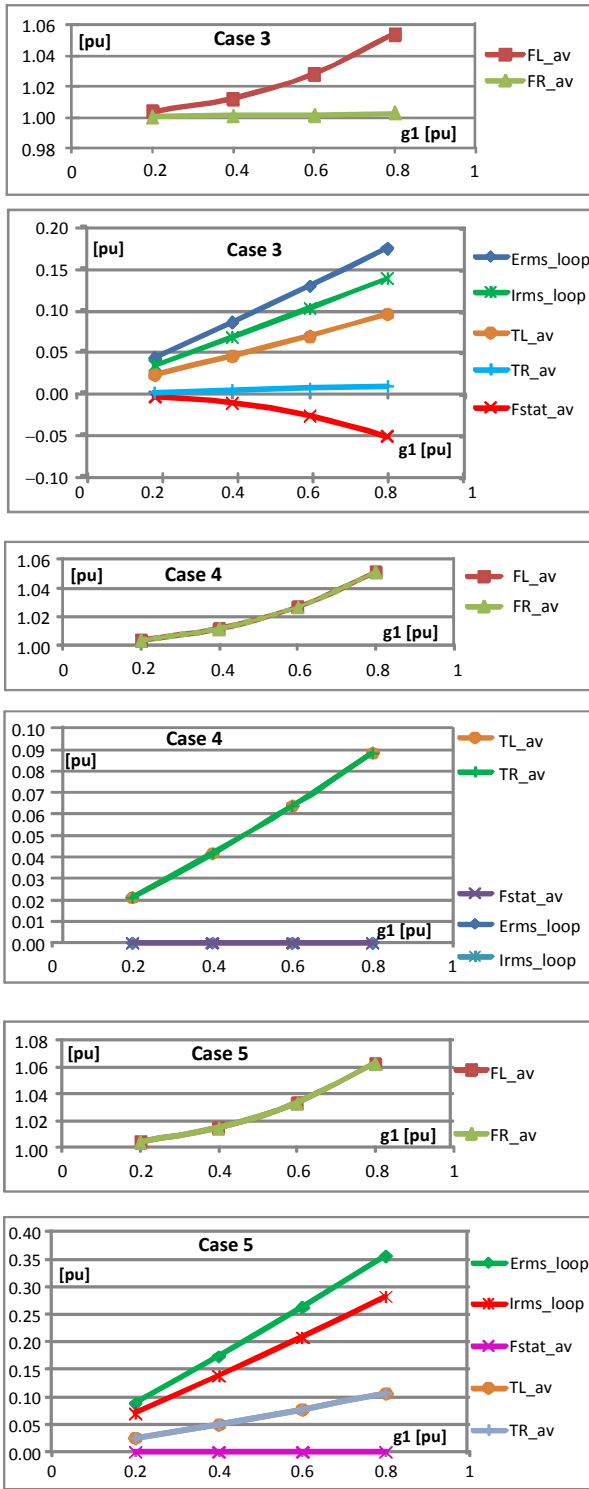
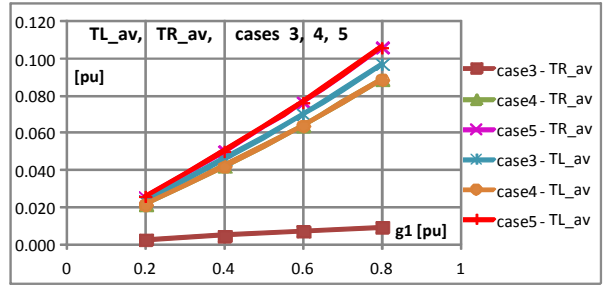Fig. 26. Evaluated quantities, as a function of tilt g_1, in cases 3, 4, 5.

Fig. 27. Linear behavior of T_{L_av}, T_{R_av} as a function of the tilt g_1, when only tilts exist (cases 3, 4, 5). When only one tilt exists (case 3), the torque occurs in practice only on the inclined disk. In all cases, the slope of both the average p.u. torque curves T_{L_av}, T_{R_av} is about 0.13.
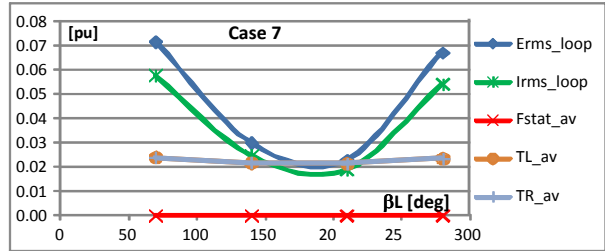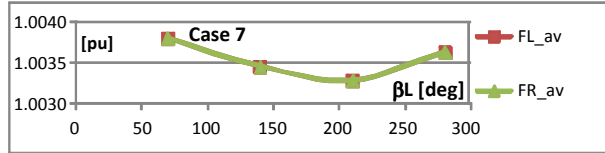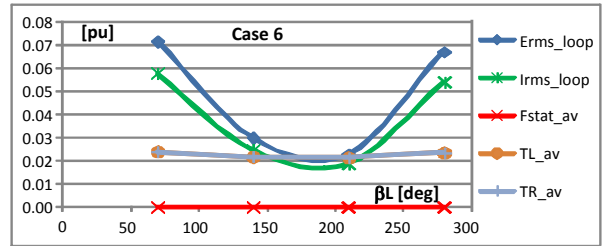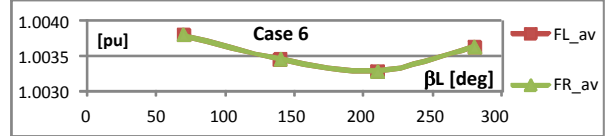

Fig. 28. Evaluated quantities, as a function of phase $β_L$ of the maximum tilt, in cases 6, 7.

VIII. CONCLUSION

Starting from an accurate reconstruction of the air gap field, some effects of manufacturing imperfections in concentrated coil axial flux PM machines have been analyzed. In particular, the currents circulating in the parallel paths at no load have been calculated, and compared with the test measurements. Moreover, the stresses, the forces, and the bending torques acting on the rotor disks and on the shaft have been evaluated and compared to 3D FEM simulation results. Finally, some simulations in the loaded operation as generator have been performed. The main conclusions are as follows:

−EMFs and circulating currents are low, except in the case of very high defect levels;

−manufacturing imperfections produce additional strengths:

disk tilts and air gap offsets cause bending torques on the disks and a resultant axial force on the stator, respectively;
- the resultant torque due to the tilts is affected by a significant ripple which should be accurately considered, because of a fatigue loading risk on shaft and disks;
- loaded operation with a stator MMF in quadrature with the PM MMF gives results similar to those concerning the no load operation.

IX. References

[1] S. Huang, J. Luo, F. Leonardi and T.A. Lipo, "A comparison of power density for axial flux machines based on the general purpose sizing equation," *IEEE Trans. Energy Convers.*, 1999, 14, (2), pp. 185-192.

[2] K. Sitapati, R. Krishnan, "Performance Comparisons of Radial and Axial Field PM Brushless Machines," *IEEE Trans. on Industry Appl.*, Vol.37, N°5, Sept./Oct. 2001, pp.1219-1226.

[3] D.G. Dorrell, M. Popescu, D.M. Ionel, "Unbalanced Magnetic Pull Due to Asymmetry and Low-Level Static Rotor Eccentricity in Fractional-Slot Brushless Permanent-Magnet Motors With Surface-Magnet and Consequent-Pole Rotors," *IEEE Trans. on Magn.*, vol.46, no.7, July 2010, pp.2675-2685.

[4] D.G. Dorrell, Hsieh Min-Fu, Guo Youguang, "Unbalanced Magnet Pull in Large Brushless Rare-Earth Permanent Magnet Motors With Rotor Eccentricity," *IEEE Trans. on Magn.*, vol.45, no.10, Oct. 2009, pp.4586-4589.

[5] Trong Duy Nguyen; King-Jet Tseng; Shao Zhang; Hoan Thong Nguyen, "A Novel Axial Flux Permanent-Magnet Machine for Flywheel Energy Storage System: Design and Analysis," *Industrial Electronics, IEEE Trans. on*, vol.58, no.9, pp.3784-3794, Sept. 2011.

[6] A. Di Gerlando, G. Foglia, M. F. Iacchetti, R. Perini, "Axial Flux PM Machines with Concentrated Armature Windings: Design Analysis and Test Validation of Wind Energy Generators," *Industrial Electronics, IEEE Trans. on*, vol.58, no.9, pp.3795-3805, Sept. 2011.

[7] R. Di Stefano and F. Marignetti, "Electromagnetic analysis of axial-flux permanent magnet synchronous machines with fractional windings with experimental validation," *IEEE Trans. Ind. Electron.*, 2012, 59, (6), pp. 2573-2582.

[8] J.F. Gieras, R.J. Wang, M.J. Kamper, "Axial Flux Permanent Magnet Brushless Machines", (Second Edition) the Springer, 375 pp, ISBN 978-1-4020-6993-2, 2008.

[9] H. Kierstead, R.-J. Wang, M.J. Kamper, "Design optimization of a single-sided axial flux permanent magnet in-wheel motor with double-layer non-overlap concentrated winding", Southern African Universities Power Engineering Conference, pp.36-40, 2009, Stellenbosch.

[10] R.J. Wang, M.J. Kamper, K. Van der Westhuizen, J.F. Gieras, "Optimal design of a coreless stator axial flux permanent magnet generator," *IEEE Trans. on Mag.*, USA, 41, No 1, 2005, pp. 55-64.

[11] D.N. Mbidi, K. van der Westhuizen, R. Wang, M.J. Kamper, J. Blom, "Mechanical design considerations of a double stage axial-flux PM machine," *Industry Applications Conference, 2000. Conference Record of the 2000 IEEE*, vol. 1, pp.198-201 vol.1, 2000.

[12] W. Fei, P.C.K. Luk, T.S. El-Hasan, "Rotor Integrity Design for a High-Speed Modular Air-Cored Axial-Flux Permanent-Magnet Generator," *Industrial Electronics, IEEE Trans. on*, vol.58, no.9, pp.3848,3858, Sept. 2011; doi: 10.1109/TIE.2011.2106097

[13] S.M. Mirimani, A. Vahedi, F. Marignetti, "Effect of Inclined Static Eccentricity Fault in Single Stator-Single Rotor Axial Flux Permanent Magnet Machines," *Mag., IEEE Trans. on*, vol.48, no.1, pp.143,149, Jan. 2012; doi: 10.1109/TMAG.2011.2161876.

[14] M. Andriollo, M. De Bortoli, G. Martinelli, A. Morini, A. Tortella, "Analysis of the air gap asymmetry in axial-flux permanent magnet generators," IEEE Electric Machines and Drives Conference, IEMDC '09, 3-6 May 2009, pp. 344-351, doi: 10.1109/IEMDC.2009.5075228.

[15] A. Di Gerlando; G. M. Foglia; M. F. Iacchetti; R. Perini; "Evaluation of Manufacturing Dissymmetry Effects in Axial Flux Permanent-Magnet Machines: Analysis Method Based on Field Functions," *Mag., IEEE Trans. on*, vol.48, no.6, pp.1995-2008, June 2012.

[16] A. S. Mc Donald, M. A. Mueller, D. E. Macpherson, "Structural analysis of low-speed axial-flux permanent-magnet machines," *IEE Proc. Electr. Power Appl.*, vol. 152, no. 6, Nov. 2005, pp. 1417-1426.

[17] A. S. McDonald, M. A. Mueller, H. Polinder, "Structural mass in direct-drive permanent magnet electrical generators," *Renewable Power Generation, IET*, vol.2, no.1, pp.3-15, March 2008.

[18] J. Lee and N. Kikuchi, "Structural topology optimization of electrical machinery to maximize stiffness with body force distribution," *IEEE Trans. Magn.*, vol. 46, no. 10, pp. 3790–3794, Oct. 2010.

[19] H. Vansompel, P. Sergeant, L. Dupré, "Optimized Design Considering the Mass Influence of an Axial Flux Permanent-Magnet Synchronous Generator With Concentrated Pole Windings," *Mag., IEEE Trans. on*, vol.46, no.12, pp.4101-4107, Dec. 2010.

[20] A. S. Mc Donald, M. A. Mueller, "Mechanical design tools for low speed high torque electrical machines," *3rd IET Intern. Conf. on Power Electronics, Machines and Drives*, pp.666-670, Mar. 2006.

[21] A. Belahcen, A. Arkkio, "Computation of additional losses due to rotor eccentricity in electrical machines," *IET Electr. Power Appl.*, vol.4, no.4, Apr. 2010, pp.259-266.

[22] N.E. Dowling, "Mechanical behaviour of materials", 3rd Edition, Prentice Hall, 2007.

[23] R.J. Wang, M.J. Kamper, R.T. Dobson, "Development of a thermofluid model for axial field permanent-magnet Machines," *Energy Conversion, IEEE Trans. on*, vol.20, no.1, pp.80,87, March 2005.

[24] O. de la Barriere, S. Hlioui, H. Ben Ahmed, M. Gabsi, M. Lo Bue, "3-D Formal Resolution of Maxwell Equations for the Computation of the No-Load Flux in an Axial Flux Permanent-Magnet Synchronous Machine," *Mag., IEEE Trans. on*, vol.48, no.1, pp.128-136, Jan. 2012.

[25] J.Y. Choi, S.H. Lee, K.J. Ko, and S.M. Jang, 'Improved analytical model for electromagnetic analysis of axial flux machines with double-sided permanent magnet rotor and coreless stator windings', *IEEE Trans. Magn.*, 2011, 47, (10), pp. 2760-2763.

[26] A. Di Gerlando, G.M. Foglia, R. Perini: "Analytical calculation of the air gap magnetic field in salient-pole three-phase synchronous machines with open slots"; Electromagnetic Fields in Mechatronics, Electrical and Electronic Engineering, IOS Press, 2006, Vol. 27, pp. 312-318; ISBN 1-58603-627-0.

[27] Z. Q. Zhu, D. Howe and C. Chan, "Improved analytical model for predicting the magnetic field distribution in brushless permanent– magnet machines," *IEEE Trans. Magn.*, Vol. 38, No.1, Jan. 2002, pp. 124-135.

[28] D. Zarko, D. Ban, T. Lipo, "Analytical calculation of magnetic field distribution in the slotted air gap of a surface permanent-magnet motor using complex relative air gap permeance," *IEEE Trans. Magn.*, Vol. 42, No. 7, July 2006, pp. 1828-1837.

[29] Z. J. Liu, J. T. Li, "Analytical solution of air gap field in PM motors taking into account the effect of pole transition over slots," *IEEE Trans. Magn.*, Vol. 43, No. 10, Oct. 2007, pp. 3872 – 3883.

[30] A. Di Gerlando, G. M. Foglia, M. F. Iacchetti, R. Perini, "Effects of Manufacturing Dissymmetry in Axial Flux PM Machines" *IEEE Intern. Conf. on Electrical Machines*, ICEM '12, Sept. 2012, Marseille – France.

[31] A.M. EL-Refaie, "Fractional-Slot Concentrated-Windings Synchronous Permanent Magnet Machines: Opportunities and Challenges", *IEEE Trans. Ind. Electron.*, vol.57, no.1, Jan. 2010, pp.107-121.

[32] A. Di Gerlando, G. Foglia, M. F. Iacchetti, R. Perini: "Analysis and Test of Diode Rectifier Solutions in Grid-Connected Wind Energy Conversion Systems Employing Modular Permanent-Magnet Synchronous Generators," *Industrial Electronics, IEEE Trans. on*, vol.59, no.5, pp.2135-2146, May 2012.